Closed-Loop Navigation of a Kinetic Zone Diagram for Redox-Mediated Electrocatalysis Using Bayesian Optimization, a Digital Twin, and Automated Electrochemistry

Michael A. Pence,[1,2] Gavin Hazen,[1,2] Joaquín Rodríguez-López[1,2*]

[1] Beckman Institute for Advanced Science and Technology, University of Illinois Urbana-Champaign, Urbana, Illinois 61801, United States

[2] Department of Chemistry, University of Illinois Urbana-Champaign, Urbana, Illinois 61801, United States

*Corresponding author: joaquinr@illinois.edu

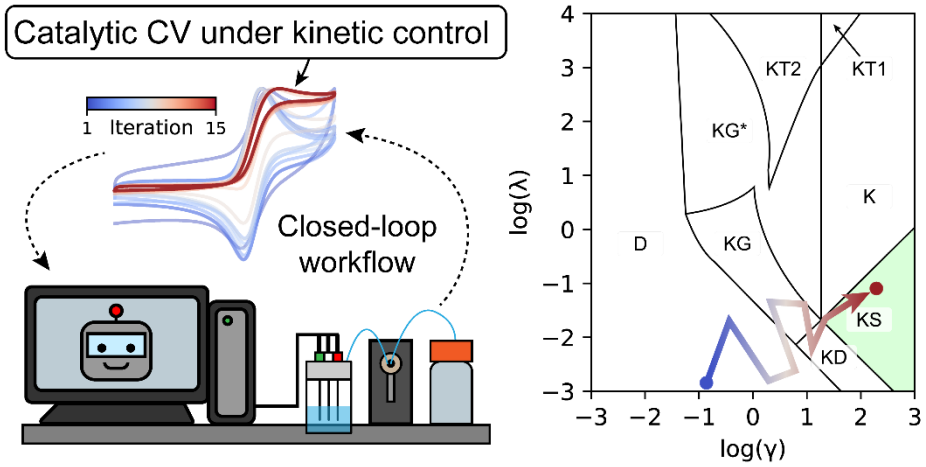

Abstract

Molecular electrocatalysis campaigns often require tuning multiple experimental parameters to obtain kinetically insightful electrochemical measurements, a prohibitively time-consuming task when performing comprehensive studies across multiple catalysts and substrates. In this work, we present an autonomous workflow that combines Bayesian optimization and automated electrochemistry to perform fully unsupervised cyclic voltammetry (CV) studies of molecular electrocatalysis. We developed CV descriptors that leveraged the conceptual framework of the EC' kinetic zone diagram to enable efficient Bayesian optimization. The CV descriptor's effect on optimization performance was evaluated using a digital twin of our autonomous experimental platform, quantifying the accuracy of obtained kinetic values against the known ground truth. We demonstrated our platform experimentally by performing autonomous studies of TEMPO-catalyzed ethanol and isopropanol electro-oxidation, demonstrating rapid identification of kinetically insightful conditions in 10 or less iterations through the closed-loop workflow. Overall, this work highlights the application of autonomous electrochemical platforms to accelerate mechanistic studies in molecular electrocatalysis and beyond.

Introduction

Electrochemistry provides a pathway to green and sustainable chemistry, enabling precise molecular transformations while minimizing environmental impact. However, many electrochemical processes require electrocatalysts to overcome large overpotentials that result from sluggish kinetics of breaking and forming bonds.[1] Molecular electrocatalysis, employing freely diffusing redox-active catalysts, provides synthetic handles to tune catalysts selectivity and activity.[2–7] Mechanistic studies of molecular electrocatalysis require extensive screening across a broad parameter space, consisting of both solution conditions and electrochemical parameters that directly impact the profile of cyclic voltammetry (CV) measurements.[8] Traditionally, this parameter space is visualized using a conceptual framework known as a kinetic zone diagram.[1,9,10] Only a subset of possible parameter combinations within such diagrams yield current-potential profiles that can be directly evaluated to obtain kinetic and mechanistic information using analytical expressions. During a comprehensive experimental campaign, where many different catalysts and substrates are evaluated, it becomes prohibitively time intensive to manually identify kinetically insightful CVs.

Autonomous experimentation with self-driving laboratories has shown the ability to accelerate lengthy experimental campaigns, reducing the time that researchers spend on tedious manual experiments.[11–13] Self-driving laboratories combine automation and machine learning (ML) to perform experiments, evaluate acquired data, and decide subsequent experimental conditions. This paradigm has been applied to a myriad of problems in fields such as organic synthesis[14–18], materials development[19–23], drug discovery[24,25], and more. Recently, autonomous experimentation in electrochemistry has begun to emerge, with self-driving labs being used for mechanistic investigations[26] and materials discovery.[27–29] This recent emergence of autonomous experiments in electrochemistry has been driven by mainstream acceptance of ML[30–35] and automation[36–43] across the community as tools that complement chemical intuition.

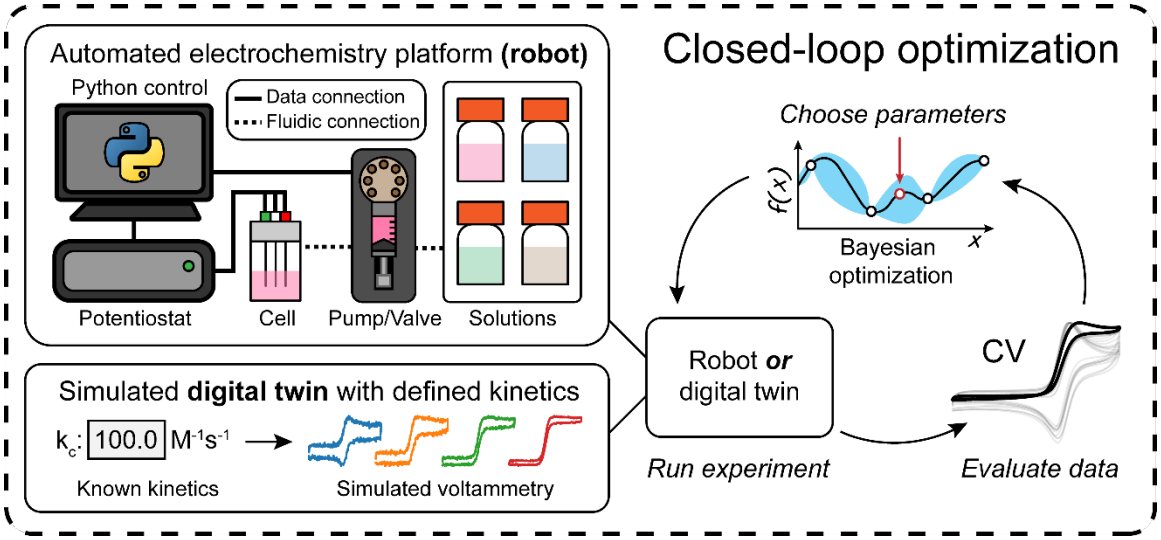

Figure 1. *Schematic of the closed-loop autonomous workflow. The workflow can be carried out with an automated electrochemistry platform or a simulated digital twin.*

In this work, we present an autonomous workflow **(Figure 1)** for unsupervised kinetic measurements of molecular electrocatalysis. The workflow optimizes solution conditions and electrochemical parameters to obtain kinetically insightful CVs. To achieve this, we combine our previously developed platform for automated electrocatalysis studies, the eLab[44], with a Bayesian optimization (BO) algorithm to enable fully autonomous and close-loop investigations of molecular electrocatalysis. To facilitate this, we took inspiration from traditional conceptual frameworks in molecular electrocatalysis theory to develop effective CV descriptors. We use a simulated replica of our autonomous platform—a "digital twin"—to assess the performance of our CV descriptors in the BO-driven autonomous workflow. We experimentally demonstrated our autonomous workflow for TEMPO catalyzed alcohol electro-oxidation, comparing the BO guided experiments to a random sampling strategy and evaluating the effects that reaction kinetics have on BO performance.

Background

CV is a widely used experimental technique for determining reaction kinetics in molecular electrocatalysis.[45–48] Here we consider the simplest case of a molecular electrocatalysis reaction, the EC' mechanism, where E is an electron transfer step at the electrode surface and C' is a catalytic reaction in solution. In the oxidative EC' mechanism shown in **Scheme 1**, the redox-active catalyst (R) is oxidized to its active form (O), which reacts with a substrate (S) to form the product (P). The catalyst, R, is regenerated during the reaction defined by the bimolecular rate constant k_c.

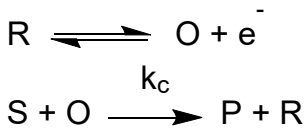

Scheme 1. Reaction scheme of a single electron oxidative EC' mechanism.

Regeneration of the catalyst during an EC' reaction produces CVs with enhanced catalytic currents, with the magnitude and profile of the resulting current-potential curve reflecting the rate of the catalytic reaction. However, directly determining the reaction rate constant from the catalytic current requires that the reaction is under kinetic control and with negligible consumption of the substrate (i.e., pseudo first-order conditions).[49] CVs under kinetic control can be visually identified by their distinctive sigmoidal current-potential profiles. Experimentally, obtaining the desired CV profile requires exploring a parameter space of various catalyst concentrations, substrate concentrations, and scan rates. Manual optimization of experimental parameters can be simplified through use of the kinetic zone diagram for the EC' mechanism, shown in **Figure 2.**

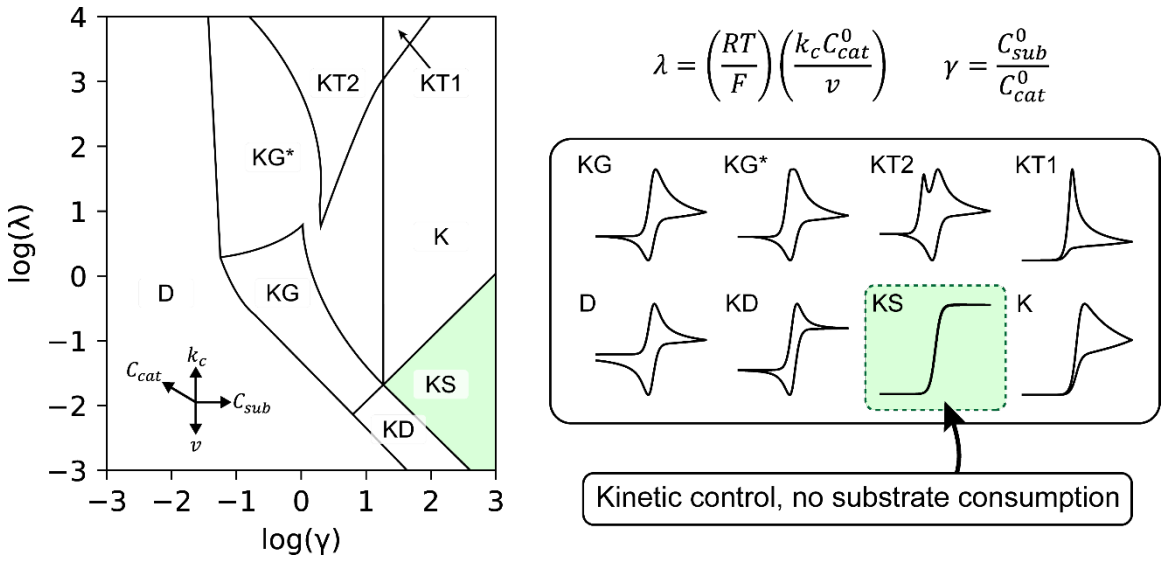

Figure 2. *Kinetic zone diagram for an EC' reaction,*[50] *with corresponding CV profiles for the different kinetic regimes.* C_{cat} *is the bulk catalyst concentration,* C_{sub} *is the bulk substrate concentration,* k_c *is the catalytic rate constant, and* ν *is the scan rate. Expressions for dimensionless parameters* λ *and* γ *are built using these variables. The KS zone is highlighted, showing the typical sigmoidal CV from which direct quantification of kinetic parameters using Equation 5 can be achieved.*

The kinetic zone diagram in **Figure 2** acts as a 'map', providing an intuitive visual description of how parameter changes affect the CV profile. It serves as a guide for parameter selection, allowing researchers to perform experiments in kinetically relevant regimes (e.g., the KS zone) where catalytic rate constants can be reliably determined. The dimensionless parameters λ **(equation 1)** and γ **(equation 2)** are the kinetic and substrate excess factors, respectively:

$$\lambda = \left(\frac{RT}{F}\right)\left(\frac{k_c C^0_{cat}}{v}\right) \quad (1)$$

$$\gamma = \frac{C^0_{sub}}{C^0_{cat}} \quad (2)$$

where *F* is Faraday's constant, *R* is the ideal gas constant, *T* is temperature, C_{cat} is the bulk catalyst concentration, C_{sub} is the bulk substrate concentration, k_c is the catalytic rate constant, and ν is the scan rate. The KS zone complies with requirements of kinetic control and negligible substrate consumption. The catalytic current, i_{pl}, is taken at the plateau region of the current-potential curve and can be used to determine the catalytic rate constant using **equation 3:**

$$i_{pl} = nFAC^0_{cat}\sqrt{Dk_{obs}C^0_{sub}} \quad (3)$$

where *n* is the number of electrons transferred in the catalytic cycle, *A* is the electrode surface area, *D* is the diffusion coefficient of the catalyst (typically assumed to be equal

to the diffusion coefficient of the substrate), and k_{obs} is the observed rate constant ($k_{obs} = k_c C_{sub}$). The need for the values of *D, A,* and C_{cat} can be removed by dividing **equation 3** by the Randles-Ševčík equation (**equation 4):**

$$i_p = 0.4463 n' F A C_{cat}^0 \sqrt{\frac{n' F v D}{RT}} \quad (4)$$

Where i_p is the peak current of the catalyst CV in the absence of substrate and *n*' is the number of electrons transferred to the catalyst. Dividing the i_{pl} by i_p gives **equation 5:**

$$\frac{i_{pl}}{i_p} = \frac{n}{0.4463 n'} \sqrt{\frac{RT k_{obs}}{n' F v}} \quad (5)$$

This approach has been extended to complex multi-electron and multi-step reactions.[51–53] The original report on the kinetic zone diagram by Su and Savéant[50] was formulated for single-electron EC' mechanisms, however the concepts and trends are generalizable to other systems. For example, an ECEC' system was experimentally tuned to navigate across all kinetic regimes of the kinetic zone diagram.[54] The generalizability and intuitive encoding of the complex relationship between CV profiles and experimental conditions has made the kinetic zone diagram an indispensable tool for electrochemists. Because of the usefulness of kinetic zone diagrams in manual electrochemistry experiments, we sought to rethink the concept in the context of autonomous electrochemistry.

Results and discussion

Rethinking the Kinetic Zone Diagram for Autonomous Experiments

The conventional framework of the kinetic zone diagram revolves around the discretization of all possible CV profiles into a small number of zones, with the boundary lines judiciously chosen based on key features of the dimensionless CV, such as peak widths, peak heights, and half-wave potentials.[50] However, the discrete nature of the kinetic zone diagram fails to reflect the continuous change in the CV profile across the parameter space.[55] Because of this, CV profiles at zone boundaries are difficult to classify due to mixed identifying features. To this end, we sought to develop CV descriptors that would capture the continuous nature of the zone diagram, enabling optimization for kinetically insightful CVs in the KS zone.

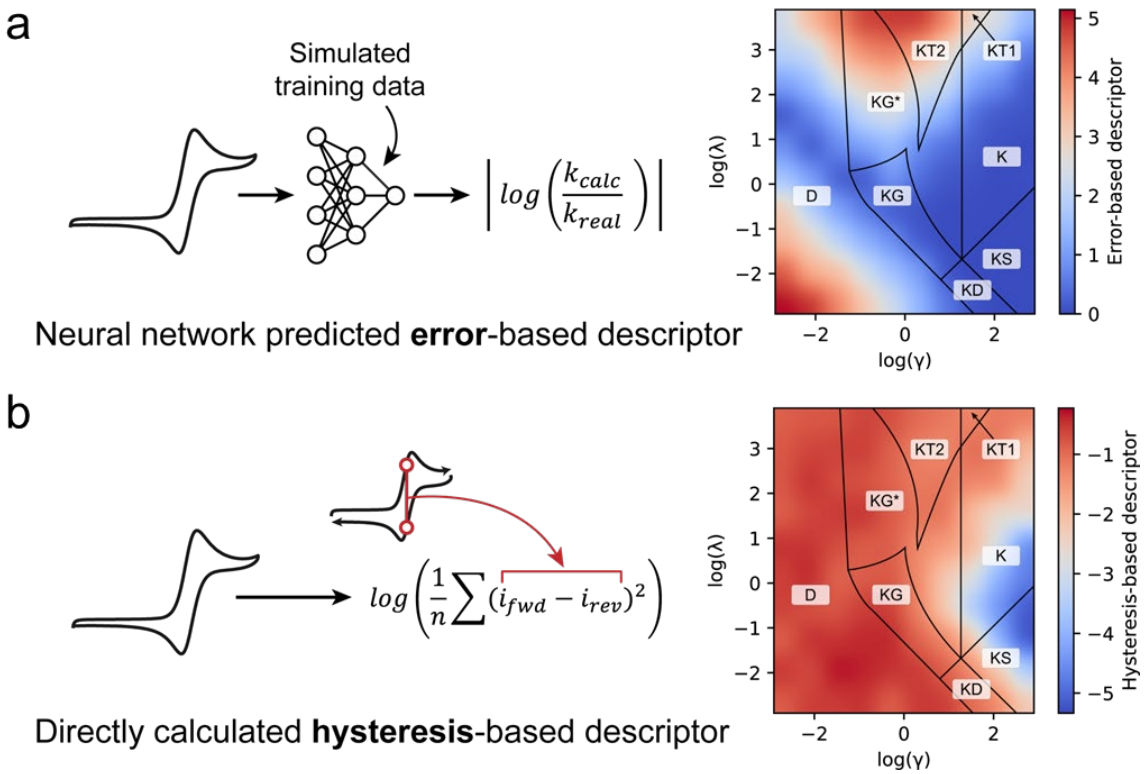

Figure 3. *Proposed descriptors and their corresponding responses over the kinetic zone diagram.* ***(a)*** *An error-based descriptor that uses a neural network trained on simulated CVs to predict the deviation between the calculated and real reaction rate constant.* ***(b)*** *A hysteresis-based descriptor calculated from the mean squared error of the forward and reverse scans of the CV.*

We developed two descriptors that seek to describe the identifying features of kinetically insightful CVs as quantifiable values. The error-based descriptor **(Figure 3a)** quantifies the accuracy of rate constants calculated using **equation 5**. The hysteresis-based descriptor **(Figure 3b)** measures differences between forward and reverse scans, owing to the negligible CV hysteresis seen when under pure kinetically controlled conditions (KS zone). The error-based descriptor is calculated from **equation 6** as:

$$Error = \left|\log\left(\frac{k_{calc}}{k_{real}}\right)\right| \quad (6)$$

where k_{calc} is the rate constant calculated using **equation 5**, and k_{real} is the true rate constant. The values of k_{real} are only known precisely through simulations however, necessitating a predictive model to attain the error-based descriptor for experimental data. We trained a neural-network regressor on simulated CVs to predict the error values described in **equation 6** for cases where the catalytic rate constant is not known (i.e., experimental measurements). The neural network employed a multi-layer perceptron architecture with a single hidden layer containing 192 units. This lightweight architecture was chosen for its balance between model complexity and training efficiency. A dropout layer (10% probability) additionally mitigated overfitting. Further details on the simulated training data, model architecture, training, and performance are provided in the **Methods**

section. Mapping the response of the error-based descriptor across the kinetic zone diagram **(Figure 3a)** revealed unexpected behavior. KS and KD zones are traditionally thought to be the only kinetic regimes where **equation 5** is applicable, however there is a thin region passing through the KG and D zones where the rate constant can be calculated within ± 10% error. This region is not practically useful for kinetic analysis however, as it is an artifact of measuring catalytic current at the switching potential for CVs that do not possess plateau-like behavior **(Figure S1).** This unanticipated region of low error presents complications for autonomous experiments, as optimization becomes more difficult if more local minima exist.

The second descriptor is a hysteresis-based measure that quantifies the difference between the forward and reverse scan, shown in **Figure 3b.** This descriptor is inspired by the minimal hysteresis and characteristic shape of the KS zone voltammograms. Unlike the error-based descriptor, this approach does not require any pre-training of a model and can be calculated directly from experimental data using **equation 7:**

$$(7) \qquad Hysteresis = log\left(\frac{1}{N}\sum(i_{fwd} - i_{rev})^2\right)$$

where N represents the number of data points in each CV sweep segment, and i_{fwd} and i_{rev} represent current on the forward and reverse sweep, respectively. Mapping hysteresis across the kinetic zone diagram reveals a well-defined minimum in the KS zone. This well-defined response surface should improve optimization performance, allowing the BO algorithm to home in on the desired CV profile. Additionally, optimizing for minimal hysteresis helps avoid CVs with substantial non-faradaic backgrounds, which can contribute to errors in determining kinetic parameters. We hypothesized that the hysteresis-based descriptor, with its simplified operation and clearly defined minima will enable faster and more consistent convergence to the desired CV profile than the error-based descriptor, allowing for more efficient autonomous experiments. We now turn to evaluate the performance of both CV descriptors using a simulated version of our autonomous workflow.

Evaluating CV Descriptor via a Digital Twin

We created a digital twin of our autonomous workflow by coupling BO to COMSOL, enabling autonomous finite element simulations **(Figure 4a).** The finite element simulations incorporating parameters C_{cat}, C_{sub}, and ν were coupled with BO, with nearly identical parameter constraints as our automated electrochemistry platform used further on. We used the digital twin to evaluate the performance of our CV descriptors, where we compared k_c values calculated from **equation 5** to the ground truth k_c values that were input into the simulation. Additionally, we incorporated simulated measurement artifacts to ensure our descriptors were robust to practical experimental conditions. In this fully autonomous workflow, simulated experiments are automatically run, analyzed, and the next parameters to sample are suggested by the BO algorithm.

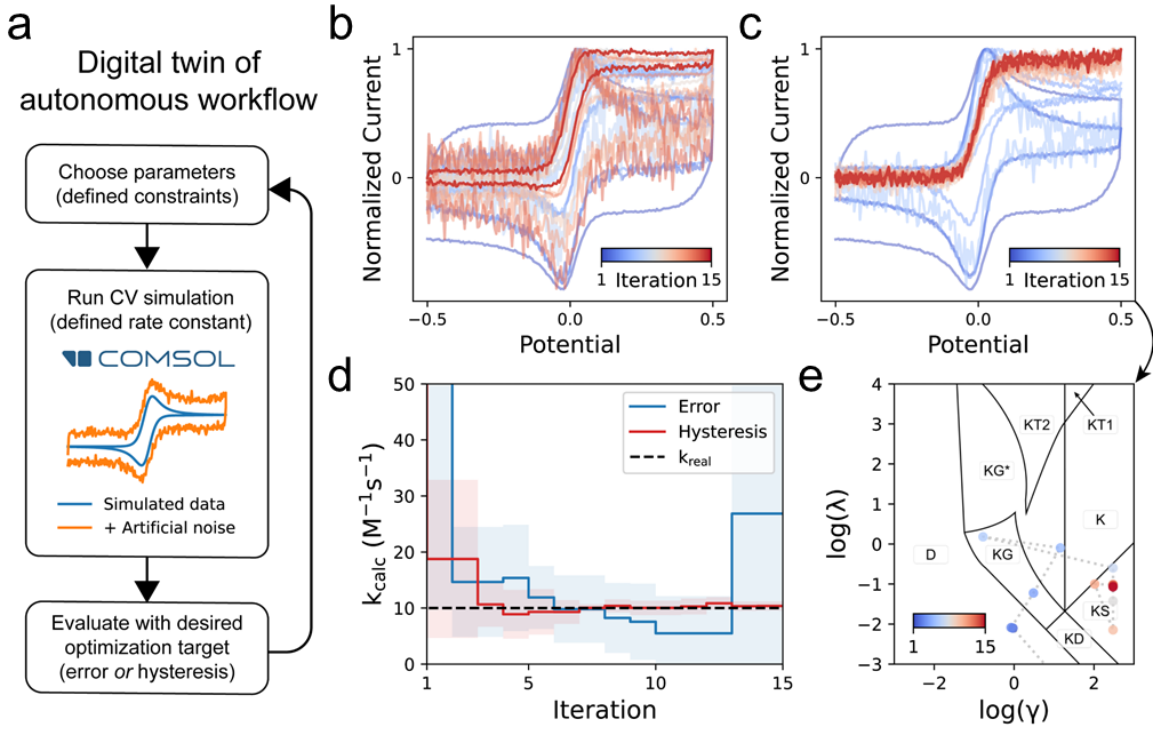

Figure 4. *Evaluating CV descriptors with a digital twin of the autonomous workflow. Data shown is from simulations where k_{real} = 10 $M^{-1}s^{-1}$. (a) Schematic of the digital twin closed-loop workflow. (b) Normalized CVs collected during BO using the error-based descriptor as the optimization target. (c) Normalized CVs collected during BO using the hysteresis-based descriptor as the optimization target. (d) Average rate constants calculated using* ***equation 5*** *for the most optimal CV at each iteration. The shaded error bars represent ± 1 standard deviation from the mean (N=5). (e) Dimensionless simulation parameters for each iteration of (c) plotted across the kinetic zone diagram.*

We tested both the error-based and hysteresis-based descriptors by performing 15-iteration autonomous experiments, with k_{real} spanning seven orders of magnitude **(Supplementary Note SNB** and **Figure S2)**. Parameters were constrained based on practical experimental values, with C_{sub} ranging from 1 to 300 mM, C_{cat} ranging from 1 to 6 mM, and ν ranging from 1 mV/s to 5 V/s. A single point in the constrained parameter space was chosen randomly as the starting point of the autonomous experiment, and all subsequently sampled parameters were suggested by the BO algorithm. This initial seed point was the same for both descriptors characterized here, to ensure a fair comparison between methods. **Figures 4b** and **Figure 4c** show the digital twin results of two BO campaigns with true k_c = 10 $M^{-1}s^{-1}$ using the error-based and hysteresis-based descriptors, respectively. We observed that the error-based descriptor led to poor convergence and displayed unpredictable behavior as the optimization proceeded. In contrast, optimization with the hysteresis-based descriptor estimated the correct k_c value within 5% error after only 8 iterations on average **(Figure 4d).** We chose to use the hysteresis-based descriptor for all following autonomous experiments. **Figure 4e** shows the BO trajectory across the kinetic zone diagram converging onto the KS zone. **Figure S3** also shows the improved accuracy and precision of the BO method vs. a random

sampling approach for various values of k_c. These results highlight the superior performance of the hysteresis-based descriptor, supporting its use in subsequent autonomous experiments.

Applying the Autonomous Workflow to TEMPO-catalyzed Alcohol Electro-oxidation

We applied the hysteresis-based descriptor to closed-loop autonomous kinetic investigations of the TEMPO-catalyzed alcohol electro-oxidation reaction shown in **Scheme 2.** Here, TEMPO (precursor R) is oxidized at the electrode to generate $TEMPO^+$ which acts as catalyst (O), reacting with a primary or secondary alcohol (S) to convert them to the corresponding aldehydes or ketones.[56,57] This catalytic reaction regenerates TEMPO by either an additional electron transfer step or a comproportionation step which are fast. Overall, the reaction in **Scheme 2** is of practical interest for organic electrosynthesis[58,59] and biomass valorization.[60,61]

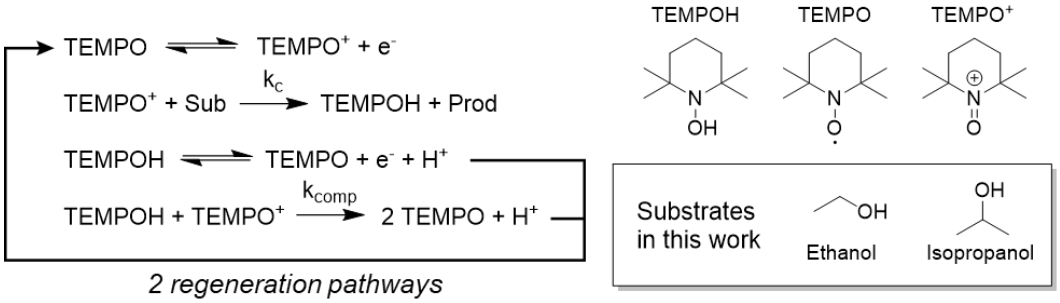

Scheme 2. *Mechanism of TEMPO-catalyzed alcohol electro-oxidation. Ethanol and isopropanol were studied as substrates in this work.*

Autonomous experiments were conducted using our previously developed eLab platform in combination with BO.[44] In brief, eLab uses opensource software to modularly interconnect a potentiostat to solution handling hardware and other peripheral instruments, enabling users to chain together multiple operations to carry out complex electrochemical experiments. A carbonate/bicarbonate buffer (pH 9.8) was selected to maintain optimal conditions for TEMPO catalysis, and a glassy carbon electrode, which is inactive towards the direct oxidation of alcohols, was used as the working electrode. Experimental parameters, including C_{cat} (1–6 mM), C_{sub} (1–300 mM), and ν (5 mV/s–5 V/s), were constrained based on practical considerations. CVs were measured by sweeping from 0 V to 0.9 V vs. Ag/AgCl and back.

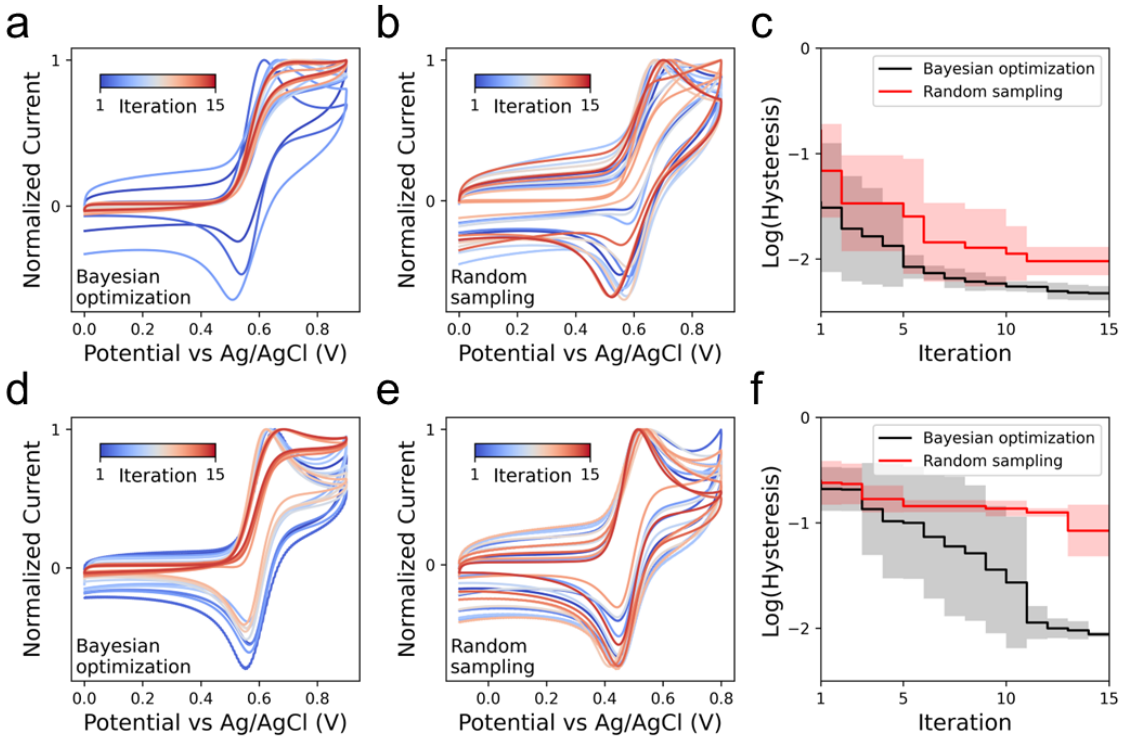

Figure 5. *Comparison of Bayesian optimization (BO) and random sampling in autonomous experiments. Ethanol (a–c) and isopropanol (d–f) were used as substrates. (a, d) Normalized CVs for BO over 15 iterations. (b, e) Normalized CVs for random sampling over 15 iterations. (c, f) Best hysteresis-based descriptor values at each iteration, averaged (N=5) with error bars showing ±1 standard deviation.*

Figures 5a and **5b** show the normalized CVs for TEMPO-catalyzed ethanol oxidation obtained from BO-guided and random sampling autonomous experiments, respectively. BO rapidly converged onto a sigmoidal profile within only a few iterations, minimizing hysteresis and yielding CVs suitable for kinetic analysis. In contrast, random sampling produced a wide variety of profiles, failing to consistently identify kinetically insightful conditions. Looking at **Figure 5c**, we see that BO is more effective at minimizing CV hysteresis in fewer iterations. Notably, BO not only outperforms random sampling, but also provides a greater fraction of CVs that would be useful for kinetic analysis.

We explored the role of reaction kinetics on BO performance by substituting ethanol with isopropanol, a secondary alcohol with slower reaction rates.[44] The normalized CVs for BO and random sampling are shown in **Figure 5d** and **5e,** respectively. The CVs for the isopropanol experiments exhibit similar behavior as observed for ethanol, however BO campaigns with isopropanol more gradually adjusted towards the optimal sigmoidal shape, likely due to the slower kinetics of this system. When we look at the average hysteresis value at each iteration for isopropanol **(Figure 5f),** we see that BO clearly outperforms random sampling. When comparing BO performance for both alcohols, we see that it takes ~10 iterations for the isopropanol trials to begin converging, as opposed to ~5 for ethanol. We attribute this to the accessible

parameter space of isopropanol having less overlap with the KS zone than ethanol, decreasing the likelihood of quickly locating a region that yields minimized hysteresis. This is evident in the random sampling experiments for isopropanol, which failed to identify CVs suitable for kinetic analysis compared to the ethanol experiments. Instead, the isopropanol random sampling experiments predominantly yield CVs in the D zone **(Figure S4)**.

Using **equation 5** (n=4 for ethanol, n=2 for isopropanol, n'=1)**,** we determined a mean k_c value of 4.2 ± 0.4 $M^{-1}s^{-1}$ and 0.243 ± 0.009 $M^{-1}s^{-1}$ for ethanol and isopropanol, respectively (N=5). These values are reasonable in comparison to prior literature for TEMPO catalyzed alcohol electro-oxidation.[57,62] We note the increased relative error observed for ethanol is likely caused by small C_{sub} values **(Figure S5)**, which require dispensing low ethanol volumes (sub 200 µL), approaching the limits of the solution handling hardware's precision. Each autonomous campaign consisted of 30 CVs each (15 in the presence of substrate to determine i_{pl}, and 15 in its absence to determine i_p) and took around 3-4 hours, depending on the chosen parameters. In between each measurement the solution was removed from the cell, flushed with water, primed with measurement solution, rinsed, and refilled. We estimate such cumbersome cleaning and dispensing regime would involve 300 unique solution dispensing and mixing operations, thus taking several experimental sessions to complete. Based on our experience, we further posit it would be more prone to dispensing and other human errors.

Conclusions

In summary, we have successfully demonstrated an autonomous, closed-loop workflow for kinetic investigations of molecular electrocatalysis using TEMPO-mediated alcohol electro-oxidation as a benchmark system. We leveraged the conceptual framework of the EC' kinetic zone diagram to derive effective CV descriptors, enabling the identification of kinetically insightful current-potential profiles. We evaluated the performance of the Bayesian optimization algorithm using first a digital twin of our autonomous platform built upon finite element method simulations incorporating likely experimental artifacts and constraints. We then combined Bayesian optimization and automated electrochemistry to perform fully autonomous, closed-loop kinetic studies of the TEMPO-alcohol system for ethanol and isopropanol. Our autonomous workflow identified conditions yielding kinetically insightful current-potential profiles in 10 iterations or less, outperforming random sampling, and reliably performing extensive solution handling and electrochemical operations, thus minimizing human involvement and error.

This work showcases integration of machine learning and automation with experimental electrochemistry, paving the way for future high-throughput kinetic studies of molecular electrocatalysts across large scopes of catalysts and substrates. In this work we demonstrated BO of a hysteresis-based descriptor which dramatically outperformed random sampling, as well as BO with an error-based descriptor. We acknowledge there could be improvements to the error-based descriptor by improving the underlying neural network model. To this end, we provide the community with a ~25,000 simulated CV

training data set to do their own explorations. We note that the methodology developed in this work can be applied to systems beyond molecular electrocatalysis, providing a general workflow to optimize CV experimental parameters for systems in energy conversion, electrosynthesis, bio-electrocatalysis, and more. The flexibility of our autonomous workflow is complemented by the modularity of our eLab[44] and Electrolab[37] platforms, which allows experimental control of temperature, gas sparging, pH, in addition to electrochemical functions beyond CV, thus enabling extremely detailed mechanistic studies without overbearing the user. Additionally, the small footprint of the solution-handling hardware (5.6”×5”×1.8”) enables easy incorporation into more complex setups, such as those controlling inert environments or coupling with spectroscopic modes of analysis.[14,49,63] We believe that the integration of machine learning and automation with electrochemistry will accelerate the discovery of new molecules and materials for a greener and more sustainable future.

Experimental

Chemicals and materials

Isopropanol (ACS grade) was purchased from Macron. TEMPO (2,2,6,6-tetramethyl-1-piperidinyloxy, 98%) was purchased from Sigma-Aldrich. Ethanol (USP grade) was purchased from Decon Labs. Sodium bicarbonate (ACS grade) was purchased from Avantor. Anhydrous sodium carbonate (ACS grade) was purchased from VWR. DI water was obtained from a Milli-Q purification system.

Software

Python 3.10.2 was used to write and execute all underlying code. A variety of Python libraries were employed to implement the autonomous workflow and support data analysis, visualization, and machine learning tasks. Key libraries include NumPy (1.26.4), pandas (1.4.3), Pytables (3.9.2), and matplotlib (3.5.1) for visualizing results. MPh (1.1.5) was employed to interface with COMSOL Multiphysics for simulating electrochemical reactions and generating training data. Machine learning components, including neural network training, were implemented using Keras/TensorFlow (2.15.0) and scikit-learn (1.1.1). For Bayesian optimization, the GPyOpt (1.2.6) library was used alongside its dependency GPy (1.13.1) for Gaussian process modeling. We note that at the time of writing, support for GPyOpt has been discontinued, and alternative libraries may be considered in future work. Custom libraries developed for this study, hardpotato (1.3.13) and elabAPI (1.1.0), were used to control the potentiostat[64] and manage solution handling[44], respectively. These custom libraries are publicly available on our GitHub repository: https://github.com/jrlLAB.

Generating simulated training data

Simulated training data was generated using COMSOL Multiphysics 5.4 with the Electrochemistry module **(Supplemental Note SN1)**. All simulations were of the EC’ mechanism **(Scheme 1)**, with varied kinetics, potential windows, diffusion-coefficients, n-

values, and initial species concentrations**.** Parameters were generated randomly in Python **(Figure S6)**. COMSOL simulations were executed through Python, using the MPh Python library (1.1.5) to interface with COMSOL. A total of 25,089 simulated CVs were generated, along with the corresponding baseline CVs in the absence of substrate. The error-based descriptor was calculated for all CVs **(equation 6).** The data was down sampled via interpolation to 400 points, ensuring uniform timesteps. Noise, capacitance, and tailing representative of solvent breakdown were added to all simulations using Python **(Figure S7).** The current values of the CVs were normalized and unfolded, and the resulting 400-element vector **(Figure S8)** was used to train the neural network model.

Creating the neural network regression model

The simulated data was used to train a neural network to predict the error-based descriptor. The 400-element vector of normalized current values were used as input features, and the calculated error-based descriptor was used as the label. Training data was split into 80% train and 20% test sets with variances in error-based descriptor of 3.685 and 3.688, respectively. The mean squared error of a validation set (10% split of train set) was used as the loss function, which was optimized using Adam's optimizer. The neural network had a multi-layer perceptron architecture with a single hidden layer, with a dropout layer prior to the output (10% probability). The hyper-parameters for the model consisted of the number of units in the hidden layer, the activation function of the hidden layer units, and the learning rate of the Adam's optimizer. Hyper-parameters were tuned with a Bayesian-optimization based tuner for 25 trials, performing up to 10 epochs of training for each trial. The best model from the Bayesian-optimization campaign had a learning rate of 0.004, a sigmoidal activation functions, and 192 units in the hidden layer **(Figure S9).** The optimized model then trained for additional 817 epochs with early stopping **(Figure S10, Figure S11, Table ST2).**

Bayesian optimization

Bayesian optimization (BO) was employed to minimize hysteresis-based and error-based descriptor values. A gaussian process was used as the surrogate model. A Lower Confidence Bound acquisition function was used with an exploration-exploitation trade-off parameter (λ) of 1 was selected, unless otherwise noted. Hyperparameters of the gaussian process, including kernel type and noise level, were estimated via maximum likelihood optimization at each iteration. The parameter domain was sampled on a log scale.

Digital Twin and Automated COMSOL Simulations

A digital twin, implemented via COMSOL Multiphysics simulations, was used to evaluate the Bayesian optimization algorithm. Simulated CVs incorporated realistic noise, non-faradaic background, and solvent breakdown to mimic experimental artifacts, ensuring robust validation of the optimization framework. Possible scan rates ranged from 1 mV/s to 5 V/s. Both catalyst and substrate concentrations for both catalyst and substrate had a

lower bound of 1 mM and had upper bounds of 6 mM and 300 mM, respectively. They were additionally constrained by **equation 8:**

$$\frac{C_{cat}}{C_{cat,stock}} + \frac{C_{sub}}{C_{sub,stock}} \leq 1 \quad (8)$$

where C_{cat} and C_{sub} are the desired concentrations of the catalyst and substrate, $C_{cat,stock}$ and $C_{sub,stock}$ are the stock concentrations of 6 mM and 300 mM respectively.

Automated Electrochemical Experiments

Automated electrochemistry experiments were performed using a modified version of our previously reported eLab platform, using a SY01B pump-valve combo to replace the separate SY08 pump and SV07 valve. All electrochemical measurements were conducted using a CH Instruments 760E bipotentiostat in a three-electrode configuration, controlled by the Hard Potato library. The setup used a 3 mm diameter glassy carbon working electrode, a graphite rod counter electrode, and an Ag/AgCl reference electrode (3 M KCl) with a salt bridge. A buffer consisting of 0.1 M sodium bicarbonate and 0.1 M sodium carbonate (pH 9.8) was used as an electrolyte. Prior to performing a set of automated experiments electrodes were preconditioned by applying an oxidative potential of 1.5 V vs. Ag/AgCl for 30 s, followed by reductive cycling from 0 V vs. Ag/AgCl to -1 V s. Ag/AgCl and back **(Figure S12).** CVs of TEMPO Experiments were performed at room temperature without gas purging, and all cyclic voltammograms are presented following the IUPAC convention. Autonomous experiments had the same concentration bounds as the digital twin, but possible scan rates were constrained between 5 mV/s and 5 V/s.

Author contributions

M.A.P.: conceptualization, data curation, formal analysis, investigation, software, methodology, visualization, writing – original draft, writing – review & editing. G.H.: methodology, software, writing – review & editing. J.R.L.: conceptualization, project administration, resources, writing – original draft, writing – review & editing.

Conflicts of interest

The authors declare no competing interest.

Data Availability

All code and data in this work including Jupyter notebooks and Python scripts for generating, processing, and analyzing the data can be found in the Zenodo repository: https://doi.org/10.5281/zenodo.14518195

Acknowledgements

This research was funded by the Beckman Institute for Advanced Science and Technology Graduate Fellows Program with support from the Arnold and Mabel Beckman

Foundation. Funding for this work was provided in part (support for G.H.) by the Robert C. and Carolyn J. Springborn Endowment.

References

(1) Savéant, J.-M.; Costentin, C. Molecular Catalysis of Electrochemical Reactions. In *Elements of Molecular and Biomolecular Electrochemistry*; John Wiley & Sons, Ltd, 2019; pp 285–381.
(2) Rein, J.; Górski, B.; Cheng, Y.; Lei, Z.; Buono, F.; Lin, S. Oxoammonium-Catalyzed Oxidation of N-Substituted Amines. *J. Am. Chem. Soc.* **2024**, *146* (46), 31412–31419. https://doi.org/10.1021/jacs.4c11758.
(3) Carneiro, S. N.; Laffoon, J. D.; Luo, L.; Sanford, M. S. Benchmarking Trisaminocyclopropeniums as Mediators for Anodic Oxidation Reactions. *J. Org. Chem.* **2024**, *89* (9), 6389–6394. https://doi.org/10.1021/acs.joc.4c00422.
(4) Mtemeri, L.; Hickey, D. P. Model-Driven Design of Redox Mediators: Quantifying the Impact of Quinone Structure on Bioelectrocatalytic Activity with Glucose Oxidase. *J. Phys. Chem. B* **2023**, *127* (36), 7685–7693. https://doi.org/10.1021/acs.jpcb.3c03740.
(5) Chalkley, M. J.; Garrido-Barros, P.; Peters, J. C. A Molecular Mediator for Reductive Concerted Proton-Electron Transfers via Electrocatalysis. *Science* **2020**, *369* (6505), 850–854. https://doi.org/10.1126/science.abc1607.
(6) Haake, M.; Reuillard, B.; Chavarot-Kerlidou, M.; Costentin, C.; Artero, V. Proton Relays in Molecular Catalysis for Hydrogen Evolution and Oxidation: Lessons From the Mimicry of Hydrogenases and Electrochemical Kinetic Analyses. *Angewandte Chemie International Edition n/a* (n/a), e202413910. https://doi.org/10.1002/anie.202413910.
(7) Teindl, K.; Patrick, B. O.; Nichols, E. M. Linear Free Energy Relationships and Transition State Analysis of CO2 Reduction Catalysts Bearing Second Coordination Spheres with Tunable Acidity. *J. Am. Chem. Soc.* **2023**, *145* (31), 17176–17186. https://doi.org/10.1021/jacs.3c03919.
(8) Savéant, J.-M. Molecular Catalysis of Electrochemical Reactions. Mechanistic Aspects. *Chem. Rev.* **2008**, *108* (7), 2348–2378. https://doi.org/10.1021/cr068079z.
(9) A. J. Bard; L. R. Faulkner; H. S. White. *Electrochemical Methods: Fundamentals and Applications*, 3rd ed.; John Wiley & Sons, Ltd: New York, 2022.
(10) Plumeré, N.; Johnson, B. A. A Geometric Interpretation of Kinetic Zone Diagrams in Electrochemistry. *J. Am. Chem. Soc.* **2024**. https://doi.org/10.1021/jacs.4c13271.
(11) Crabtree, G. Self-Driving Laboratories Coming of Age. *Joule* **2020**, *4* (12), 2538–2541. https://doi.org/10.1016/j.joule.2020.11.021.
(12) Abolhasani, M.; Kumacheva, E. The Rise of Self-Driving Labs in Chemical and Materials Sciences. *Nat. Synth* **2023**, *2* (6), 483–492. https://doi.org/10.1038/s44160-022-00231-0.
(13) Tom, G.; Schmid, S. P.; Baird, S. G.; Cao, Y.; Darvish, K.; Hao, H.; Lo, S.; Pablo-García, S.; Rajaonson, E. M.; Skreta, M.; Yoshikawa, N.; Corapi, S.; Akkoc, G. D.; Strieth-Kalthoff, F.; Seifrid, M.; Aspuru-Guzik, A. Self-Driving Laboratories for Chemistry and Materials Science. *Chem. Rev.* **2024**, *124* (16), 9633–9732. https://doi.org/10.1021/acs.chemrev.4c00055.

(14) Bell, N. L.; Boser, F.; Bubliauskas, A.; Willcox, D. R.; Luna, V. S.; Cronin, L. Autonomous Execution of Highly Reactive Chemical Transformations in the Schlenkputer. *Nat Chem Eng* **2024**, *1* (2), 180–189. https://doi.org/10.1038/s44286-023-00024-y.
(15) Li, S.; Jira, E. R.; Angello, N. H.; Li, J.; Yu, H.; Moore, J. S.; Diao, Y.; Burke, M. D.; Schroeder, C. M. Using Automated Synthesis to Understand the Role of Side Chains on Molecular Charge Transport. *Nat Commun* **2022**, *13* (1), 2102. https://doi.org/10.1038/s41467-022-29796-2.
(16) Boiko, D. A.; MacKnight, R.; Kline, B.; Gomes, G. Autonomous Chemical Research with Large Language Models. *Nature* **2023**, *624* (7992), 570–578. https://doi.org/10.1038/s41586-023-06792-0.
(17) Steiner, S.; Wolf, J.; Glatzel, S.; Andreou, A.; Granda, J. M.; Keenan, G.; Hinkley, T.; Aragon-Camarasa, G.; Kitson, P. J.; Angelone, D.; Cronin, L. Organic Synthesis in a Modular Robotic System Driven by a Chemical Programming Language. *Science* **2019**, *363* (6423), eaav2211. https://doi.org/10.1126/science.aav2211.
(18) Coley, C. W.; Thomas, D. A.; Lummiss, J. A. M.; Jaworski, J. N.; Breen, C. P.; Schultz, V.; Hart, T.; Fishman, J. S.; Rogers, L.; Gao, H.; Hicklin, R. W.; Plehiers, P. P.; Byington, J.; Piotti, J. S.; Green, W. H.; Hart, A. J.; Jamison, T. F.; Jensen, K. F. A Robotic Platform for Flow Synthesis of Organic Compounds Informed by AI Planning. *Science* **2019**, *365* (6453), eaax1566. https://doi.org/10.1126/science.aax1566.
(19) Xu, R. H. J.; Keating, L. P.; Vikram, A.; Shim, M.; Kenis, P. J. A. Understanding Hot Injection Quantum Dot Synthesis Outcomes Using Automated High-Throughput Experiment Platforms and Machine Learning. *Chem. Mater.* **2024**, *36* (3), 1513–1525. https://doi.org/10.1021/acs.chemmater.3c02751.
(20) MacLeod, B. P.; Parlane, F. G. L.; Morrissey, T. D.; Häse, F.; Roch, L. M.; Dettelbach, K. E.; Moreira, R.; Yunker, L. P. E.; Rooney, M. B.; Deeth, J. R.; Lai, V.; Ng, G. J.; Situ, H.; Zhang, R. H.; Elliott, M. S.; Haley, T. H.; Dvorak, D. J.; Aspuru-Guzik, A.; Hein, J. E.; Berlinguette, C. P. Self-Driving Laboratory for Accelerated Discovery of Thin-Film Materials. *Science Advances* **2020**, *6* (20), eaaz8867. https://doi.org/10.1126/sciadv.aaz8867.
(21) Vikram, A.; Brudnak, K.; Zahid, A.; Shim, M.; A. Kenis, P. J. Accelerated Screening of Colloidal Nanocrystals Using Artificial Neural Network-Assisted Autonomous Flow Reactor Technology. *Nanoscale* **2021**, *13* (40), 17028–17039. https://doi.org/10.1039/D1NR05497J.
(22) Salley, D.; Keenan, G.; Grizou, J.; Sharma, A.; Martín, S.; Cronin, L. A Nanomaterials Discovery Robot for the Darwinian Evolution of Shape Programmable Gold Nanoparticles. *Nat Commun* **2020**, *11* (1), 2771. https://doi.org/10.1038/s41467-020-16501-4.
(23) Szymanski, N. J.; Rendy, B.; Fei, Y.; Kumar, R. E.; He, T.; Milsted, D.; McDermott, M. J.; Gallant, M.; Cubuk, E. D.; Merchant, A.; Kim, H.; Jain, A.; Bartel, C. J.; Persson, K.; Zeng, Y.; Ceder, G. An Autonomous Laboratory for the Accelerated Synthesis of Novel Materials. *Nature* **2023**, *624* (7990), 86–91. https://doi.org/10.1038/s41586-023-06734-w.
(24) Schneider, G. Automating Drug Discovery. *Nat Rev Drug Discov* **2018**, *17* (2), 97–113. https://doi.org/10.1038/nrd.2017.232.

(25) Bailey, M.; Moayedpour, S.; Li, R.; Corrochano-Navarro, A.; Kötter, A.; Kogler-Anele, L.; Riahi, S.; Grebner, C.; Hessler, G.; Matter, H.; Bianciotto, M.; Mas, P.; Bar-Joseph, Z.; Jager, S. Deep Batch Active Learning for Drug Discovery. *eLife* **2023**, *12*. https://doi.org/10.7554/eLife.89679.
(26) Sheng, H.; Sun, J.; Rodríguez, O.; Hoar, B. B.; Zhang, W.; Xiang, D.; Tang, T.; Hazra, A.; Min, D. S.; Doyle, A. G.; Sigman, M. S.; Costentin, C.; Gu, Q.; Rodríguez-López, J.; Liu, C. Autonomous Closed-Loop Mechanistic Investigation of Molecular Electrochemistry via Automation. *Nat Commun* **2024**, *15* (1), 2781. https://doi.org/10.1038/s41467-024-47210-x.
(27) Quinn, H.; Robben, G. A.; Zheng, Z.; Gardner, A. L.; Werner, J. G.; Brown, K. A. PANDA: A Self-Driving Lab for Studying Electrodeposited Polymer Films. *Mater. Horiz.* **2024**. https://doi.org/10.1039/D4MH00797B.
(28) Kodera, M.; Sayama, K. An Automatic Robot System for Machine Learning–Assisted High-Throughput Screening of Composite Electrocatalysts. *Digital Discovery* **2023**, *2* (6), 1683–1687. https://doi.org/10.1039/D3DD00116D.
(29) Dave, A.; Mitchell, J.; Burke, S.; Lin, H.; Whitacre, J.; Viswanathan, V. Autonomous Optimization of Nonaqueous Battery Electrolytes via Robotic Experimentation and Machine Learning. *Nat Commun* **2022**, *13* (1), 5454. https://doi.org/10.1038/s41467-022-32938-1.
(30) Sun, J.; Liu, C. What and How Can Machine Learning Help to Decipher Mechanisms in Molecular Electrochemistry? *Current Opinion in Electrochemistry* **2023**, *39*, 101306. https://doi.org/10.1016/j.coelec.2023.101306.
(31) Chen, H.; Kätelhön, E.; Compton, R. G. Machine Learning in Fundamental Electrochemistry: Recent Advances and Future Opportunities. *Current Opinion in Electrochemistry* **2023**, *38*, 101214. https://doi.org/10.1016/j.coelec.2023.101214.
(32) Mistry, A.; Franco, A. A.; Cooper, S. J.; Roberts, S. A.; Viswanathan, V. How Machine Learning Will Revolutionize Electrochemical Sciences. *ACS Energy Lett.* **2021**, *6* (4), 1422–1431. https://doi.org/10.1021/acsenergylett.1c00194.
(33) Gundry, L.; Guo, S.-X.; Kennedy, G.; Keith, J.; Robinson, M.; Gavaghan, D.; Bond, A. M.; Zhang, J. Recent Advances and Future Perspectives for Automated Parameterisation, Bayesian Inference and Machine Learning in Voltammetry. *Chem. Commun.* **2021**, *57* (15), 1855–1870. https://doi.org/10.1039/D0CC07549C.
(34) Kennedy, G. F.; Zhang, J.; Bond, A. M. Automatically Identifying Electrode Reaction Mechanisms Using Deep Neural Networks. *Anal. Chem.* **2019**, *91* (19), 12220–12227. https://doi.org/10.1021/acs.analchem.9b01891.
(35) Hoar, B. B.; Zhang, W.; Chen, Y.; Sun, J.; Sheng, H.; Zhang, Y.; Chen, Y.; Yang, J. Y.; Costentin, C.; Gu, Q.; Liu, C. Redox-Detecting Deep Learning for Mechanism Discernment in Cyclic Voltammograms of Multiple Redox Events. *ACS Electrochem.* **2024**. https://doi.org/10.1021/acselectrochem.4c00014.
(36) Abed, J.; Bai, Y.; Persaud, D.; Kim, J.; Witt, J.; Hattrick-Simpers, J.; H. Sargent, E. AMPERE: Automated Modular Platform for Expedited and Reproducible Electrochemical Testing. *Digital Discovery* **2024**. https://doi.org/10.1039/D4DD00203B.
(37) Oh, I.; Pence, M. A.; Lukhanin, N. G.; Rodríguez, O.; Schroeder, C. M.; Rodríguez-López, J. The Electrolab: An Open-Source, Modular Platform for Automated

Characterization of Redox-Active Electrolytes. *Device* **2023**, *1* (5), 100103. https://doi.org/10.1016/j.device.2023.100103.
(38) Duke, R.; Mahmoudi, S.; Preet Kaur, A.; Bhat, V.; C. Dingle, I.; C. Stumme, N.; K. Shaw, S.; Eaton, D.; Vego, A.; Risko, C. ExpFlow: A Graphical User Interface for Automated Reproducible Electrochemistry. *Digital Discovery* **2024**, *3* (1), 163–172. https://doi.org/10.1039/D3DD00156C.
(39) Liang, S.; Kinghorn, A. B.; Voliotis, M.; Prague, J. K.; Veldhuis, J. D.; Tsaneva-Atanasova, K.; McArdle, C. A.; Li, R. H. W.; Cass, A. E. G.; Dhillo, W. S.; Tanner, J. A. Measuring Luteinising Hormone Pulsatility with a Robotic Aptamer-Enabled Electrochemical Reader. *Nat Commun* **2019**, *10* (1), 852. https://doi.org/10.1038/s41467-019-08799-6.
(40) Alden, S. E.; Zhang, L.; Wang, Y.; Lavrik, N. V.; Thorgaard, S. N.; Baker, L. A. High-Throughput Single-Entity Electrochemistry with Microelectrode Arrays. *Anal. Chem.* **2024**, *96* (22), 9177–9184. https://doi.org/10.1021/acs.analchem.4c01092.
(41) Zeng, J. S.; Padia, V.; Chen, G. Y.; Maalouf, J. H.; Limaye, A. M.; Liu, A. H.; Yusov, M. A.; Hunter, I. W.; Manthiram, K. Nonidealities in CO2 Electroreduction Mechanisms Revealed by Automation-Assisted Kinetic Analysis. *ACS Cent. Sci.* **2024**, *10* (7), 1348–1356. https://doi.org/10.1021/acscentsci.3c01295.
(42) Mo, Y.; Rughoobur, G.; Nambiar, A. M. K.; Zhang, K.; Jensen, K. F. A Multifunctional Microfluidic Platform for High-Throughput Experimentation of Electroorganic Chemistry. *Angew Chem Int Ed Engl* **2020**, *59* (47), 20890–20894. https://doi.org/10.1002/anie.202009819.
(43) Pablo-García, S.; García, Á.; Akkoc, G. D.; Sim, M.; Cao, Y.; Somers, M.; Hattrick, C.; Yoshikawa, N.; Dworschak, D.; Hao, H.; Aspuru-Guzik, A. An Affordable Platform for Automated Synthesis and Electrochemical Characterization. ChemRxiv February 8, 2024. https://doi.org/10.26434/chemrxiv-2024-cwnwc.
(44) A. Pence, M.; Hazen, G.; Rodríguez-López, J. An Automated Electrochemistry Platform for Studying pH-Dependent Molecular Electrocatalysis. *Digital Discovery* **2024**, *3* (9), 1812–1821. https://doi.org/10.1039/D4DD00186A.
(45) Boucher, D. G.; Pendergast, A. D.; Wu, X.; Nguyen, Z. A.; Jadhav, R. G.; Lin, S.; White, H. S.; Minteer, S. D. Unraveling Hydrogen Atom Transfer Mechanisms with Voltammetry: Oxidative Formation and Reactivity of Cobalt Hydride. *J. Am. Chem. Soc.* **2023**, *145* (32), 17665–17677. https://doi.org/10.1021/jacs.3c03815.
(46) O'Reilly, M. E.; Kim, R. S.; Oh, S.; Surendranath, Y. Catalytic Methane Monofunctionalization by an Electrogenerated High-Valent Pd Intermediate. *ACS Cent. Sci.* **2017**, *3* (11), 1174–1179. https://doi.org/10.1021/acscentsci.7b00342.
(47) Pattanayak, S.; Berben, L. A. Pre-Equilibrium Reaction Mechanism as a Strategy to Enhance Rate and Lower Overpotential in Electrocatalysis. *J. Am. Chem. Soc.* **2023**, *145* (6), 3419–3426. https://doi.org/10.1021/jacs.2c10942.
(48) McKenzie, E. C. R.; Hosseini, S.; Tanwar, M.; Neurock, M.; Minteer, S. D.; Jacobson, S. C. Mechanistic Insights into Electrocatalytic Carbon−Bromine Bond Cleavage in Polybrominated Phenols. *J. Phys. Chem. C* **2023**, *127* (35), 17335–17344. https://doi.org/10.1021/acs.jpcc.3c01506.
(49) Lee, K. J.; Elgrishi, N.; Kandemir, B.; Dempsey, J. L. Electrochemical and Spectroscopic Methods for Evaluating Molecular Electrocatalysts. *Nat Rev Chem* **2017**, *1* (5), 1–14. https://doi.org/10.1038/s41570-017-0039.

(50) Savéant, J. M.; Su, K. B. Homogeneous Redox Catalysis of Electrochemical Reaction: Part VI. Zone Diagram Representation of the Kinetic Regimes. *Journal of Electroanalytical Chemistry and Interfacial Electrochemistry* **1984**, *171* (1), 341–349. https://doi.org/10.1016/0022-0728(84)80125-4.
(51) Costentin, C.; Savéant, J.-M. Multielectron, Multistep Molecular Catalysis of Electrochemical Reactions: Benchmarking of Homogeneous Catalysts. *ChemElectroChem* **2014**, *1* (7), 1226–1236. https://doi.org/10.1002/celc.201300263.
(52) Costentin, C.; Nocera, D. G.; Brodsky, C. N. Multielectron, Multisubstrate Molecular Catalysis of Electrochemical Reactions: Formal Kinetic Analysis in the Total Catalysis Regime. *Proceedings of the National Academy of Sciences* **2017**, *114* (43), 11303–11308. https://doi.org/10.1073/pnas.1711129114.
(53) Rountree, E. S.; McCarthy, B. D.; Eisenhart, T. T.; Dempsey, J. L. Evaluation of Homogeneous Electrocatalysts by Cyclic Voltammetry. *Inorg. Chem.* **2014**, *53* (19), 9983–10002. https://doi.org/10.1021/ic500658x.
(54) Martin, D. J.; McCarthy, B. D.; Rountree, E. S.; Dempsey, J. L. Qualitative Extension of the EC′ Zone Diagram to a Molecular Catalyst for a Multi-Electron, Multi-Substrate Electrochemical Reaction. *Dalton Trans.* **2016**, *45* (24), 9970–9976. https://doi.org/10.1039/C6DT00302H.
(55) Plumeré, N.; Johnson, B. A. A Geometric Interpretation of Kinetic Zone Diagrams in Electrochemistry. ChemRxiv August 16, 2024. https://doi.org/10.26434/chemrxiv-2024-d31p4.
(56) Nutting, J. E.; Rafiee, M.; Stahl, S. S. Tetramethylpiperidine N-Oxyl (TEMPO), Phthalimide N-Oxyl (PINO), and Related N-Oxyl Species: Electrochemical Properties and Their Use in Electrocatalytic Reactions. *Chem. Rev.* **2018**, *118* (9), 4834–4885. https://doi.org/10.1021/acs.chemrev.7b00763.
(57) Mishra, A.; Kim, J.; Zorigt, M.; Romo, A. I. B.; Gaddam, R.; Braun, J. E.; Ziviani, D.; Rodríguez-López, J. Highly Selective TEMPO Catalyzed Bulk Electrooxidation of Isopropanol to Acetone for Application in Electrochemical Heat Pumping. *ACS Sustainable Chem. Eng.* **2023**, *11* (16), 6241–6249. https://doi.org/10.1021/acssuschemeng.2c07419.
(58) Siu, J. C.; Sauer, G. S.; Saha, A.; Macey, R. L.; Fu, N.; Chauviré, T.; Lancaster, K. M.; Lin, S. Electrochemical Azidooxygenation of Alkenes Mediated by a TEMPO–N3 Charge-Transfer Complex. *J. Am. Chem. Soc.* **2018**, *140* (39), 12511–12520. https://doi.org/10.1021/jacs.8b06744.
(59) Wang, Z.-H.; Gao, P.-S.; Wang, X.; Gao, J.-Q.; Xu, X.-T.; He, Z.; Ma, C.; Mei, T.-S. TEMPO-Enabled Electrochemical Enantioselective Oxidative Coupling of Secondary Acyclic Amines with Ketones. *J. Am. Chem. Soc.* **2021**, *143* (38), 15599–15605. https://doi.org/10.1021/jacs.1c08671.
(60) Carroll, E.; Parker, S. L.; Fukushima, A.; Downey, S.; Miller, D.; Nguyen, Z. A.; Boucher, D. G.; Minteer, S. D. Improved Electrosynthesis of Biomass Derived Furanic Compounds via Nitroxyl Radical Redox Mediation. *Chem Bio Eng.* **2024**. https://doi.org/10.1021/cbe.4c00034.
(61) Lucas, F. W. S.; Grim, R. G.; Tacey, S. A.; Downes, C. A.; Hasse, J.; Roman, A. M.; Farberow, C. A.; Schaidle, J. A.; Holewinski, A. Electrochemical Routes for the Valorization of Biomass-Derived Feedstocks: From Chemistry to Application. *ACS*

Energy Lett. **2021**, *6* (4), 1205–1270. https://doi.org/10.1021/acsenergylett.0c02692.
(62) Rafiee, M.; Miles, K. C.; Stahl, S. S. Electrocatalytic Alcohol Oxidation with TEMPO and Bicyclic Nitroxyl Derivatives: Driving Force Trumps Steric Effects. *J. Am. Chem. Soc.* **2015**, *137* (46), 14751–14757. https://doi.org/10.1021/jacs.5b09672.
(63) Angello, N. H.; Friday, D. M.; Hwang, C.; Yi, S.; Cheng, A. H.; Torres-Flores, T. C.; Jira, E. R.; Wang, W.; Aspuru-Guzik, A.; Burke, M. D.; Schroeder, C. M.; Diao, Y.; Jackson, N. E. Closed-Loop Transfer Enables Artificial Intelligence to Yield Chemical Knowledge. *Nature* **2024**, *633* (8029), 351–358. https://doi.org/10.1038/s41586-024-07892-1.
(64) Rodríguez, O.; Pence, M. A.; Rodríguez-López, J. Hard Potato: A Python Library to Control Commercial Potentiostats and to Automate Electrochemical Experiments. *Anal. Chem.* **2023**, *95* (11), 4840–4845. https://doi.org/10.1021/acs.analchem.2c04862.